DOI: 10.15480/882.9323

Eighth International Symposium on Marine Propulsors
smp'24, Berlin, Germany, March 2024

A Superposition Method to Evaluate the Strength of Propellers in Crushed Ice Flow Considering Collision and Hydrodynamic Load

Haiyan Wu[1,2], Jingjing Liu[1,2], Long Yu[1,2], Youjiang Wang[1,2]

[1] State Key Laboratory of Ocean Engineering, School of Naval Architecture, Ocean and Civil Engineering, Shanghai Jiao Tong University, China

[2] School of Naval Architecture, Ocean & Civil Engineering, Shanghai Jiao Tong University, Shanghai, China

ABSTRACT

Polar ships play a crucial role in the exploitation of Arctic resources, and their propellers are threatened by ice loads. Therefore, it is vital to investigate ice loads and conduct strength checks on propellers. In this study, a superposition method to evaluate the strength of propeller in crushed ice flow is established and numerical simulation methods is used to conduct research. Firstly, according to URI3, the potentially hazardous areas where crushed ice-propeller collision may occur could be determined, and the flow characteristics considering crushed ice-propeller interaction is calculated based on computational fluid dynamics (CFD)-discrete element method (DEM), and loads on blade surfaces can be extracted as input conditions in the next step. The ice in flow is unbreakable. Then, the strength analysis is completed with Finite Element Method (FEM), where pressure loads are derived from flow field calculations. The results indicate that ice particles from the front of the propeller are prone to collide with the pressure surface near the leading edge. The hydrodynamic performance of the propeller is also affected, with a decrease in propulsive efficiency in ice flow and a greater reduction with increasing advance coefficient.

Keywords

superposition method, strength check, CFD-DEM, ice, propeller ice interaction

1 INTRODUCTION

With the global climate warming, the exploitation of Arctic channel resources and natural resources holds enormous commercial potential and economic value, in which polar ships play an indispensable role. The severe environmental conditions in polar regions expose ships to the threat of ice loads, and propellers are prone to contact with ice, resulting in strength issues due to ice-propeller contact forces. Currently, research on ice-propeller contact remains a significant challenge. On the one hand, it is difficult to determine the constitutive equation of ice, as various factors such as age, thickness, and formation conditions affect the physical and mechanical properties of ice (Timco & Weeks 2010). On the other hand, the complex shape of propellers and the unpredictable nature of their contact with ice further compound the difficulty.

Regarding the problem of propeller subjected to ice interaction, two common methods are used for researches: experimentation and numerical simulation. Some researchers conducted full-scale trails. The hydrodynamic non-contact and contact loads during ice-propeller interaction, and some parametric trends are studied (Browne 1997; Newburr et al 1994; Newbury et al 1993; Williams & Spencer 1992). Meanwhile, the model-scale experiments are more practical on the controlled conditions and more precise information considering the interaction conditions (Chunyu et al 2022). Many researchers have analyzed ice milling loads, "inseparable" hydrodynamic loads, and "separable" hydrodynamic loads with designing appropriate experiments targeted at different types of propellers (Searle et al 2001; Wang et al 2019; Wang et al 2005; Wang et al 2006; Xiong et al 2022). Some researchers also improved the measuring methods for experiments.

With the advancement of information technology, numerical simulation has demonstrated a significant advantage in balancing both economy and efficiency. Many methods and techniques have been applied to the researches of interactions between ice and structures. The ship-ice interactions are highly concerned, many researches considered the ice is unbreakable. Guo et al(2018) established ship model and crushed ices using the

FEM, and predicted ice resistance of the ship under several ice concentrations. Wang et al(2020) used the arbitrary Lagrangian-Eulerian (ALE) method based on FEM to set up ship-water-air-ice coupling model, with the ice material defined as elastic. Janßen et al(2017) solved the simulation of fluid-ship-ice interactions based on the Lattice Boltzmann Method (LBM), treating the ice floes and ship as rigid bodies. Vroegrijk(2012) calculated the hydrodynamics of the ship, sailing through ice which is spherical and viscoelastic, in combination with CFD and DEM. Luo et al(2020) applied the CFD-DEM coupling numerical method to the simulation of ship-water interaction, in which the ice is unbreakable, shaped as tetrahedral and irregular polyhedral. At the same time, many scholars studied the interactions between ice and structures considering the failure of ice. Zhang et al(2019) implemented the process of ice-ship interactions based on SPH method, simulating the failure progress of layer ice with softening elastoplastic model integrating Drucker-Prager yield criterion. Chen et al(2021) simulated the processes that cone and icebreaker advance and break level ice based on FEM-SPH adaptive method. In this method, finite elements were converted into SPH particles under given conditions, then could be broken. The Peridynamic (PD) method is also used in the breaking of ice. Song et al(2019) simulated the contact between the rigid projectile and ice targets based on the PD contact algorithm, with a modified Drucker-Prager model to simulate the ice material and the technique of adaptive particle refinement was used to investigate the ice craters. Ye et al(2020) simulated the interaction between a submarine and an ice sheet, developed a contact detection method to detect the area where the submarine and ice contact happens and analyzed the characteristics of the ice failure process based on the PD. Kang et al(2023) considered carefully the standard of ice damage in the state-based PD method, including critical bond-stretch (CS) and critical energy (CE) damage criteria, and implemented a simplified two-dimensional (2D) airfoil-ice contacting model. For ships, most researches are aimed at resistance estimation, while a few works have addressed local ice loads (Li & Huang 2022). For propellers, hydrodynamic performance and strength are studied in different conditions. Heydari et al(2019) simulated an ice mass close to propeller based on CFD-DEM-Multi Body Dynamic (MBD) method, and analyzed the blockage impacts. Based on PD and contact detection method, Ye et al(2017) simulated the brittle failure behavior of the ice during propeller-ice milling. Yang et al(2023) established the ice block and propeller using the sphere-based DEM and hexahedral solid elements of the FEM, respectively, simulating the ice-propeller milling process.

Currently, the standard method is the most widely used method for strength check of ice-class propellers, mainly including a set of unified requirements (URI3) presented by the International Association of Classification Societies (IACS). On this base, Liu et al(2015) proposed an advanced 3D unsteady panel method combining the URI3 for the design and optimization of the strength of polar class propellers in both milling and impact cases. Guo et al(2021) established a strength evaluation method with FEM considering the ice load and the hydrodynamic load respectively based on the URI3 and the panel method.

In this study, a superposition method to evaluate the strength of propeller in crushed ice flow is established and the hydrodynamic performance is analyzed under different conditions. Considering a light ice condition, as the simplified spherical ice particles come from the area referred to the IACS URI3 rules and impact with propeller, the hydrodynamic performance and strength are investigated in this process at different advance coefficients. The research can provide a reference for analyzing the force conditions of propellers in crushed ice flow. The remainder of this paper is organized as follows. Firstly, the basic principles of CFD-DEM and finite element methods are introduced in Sections 2.1 and 2.2. The IACS URI3 rules concerning ice-class propellers and analysis procedure are briefly presented in Section 2.3. Next, the calculation model and loading scenarios are provided in Sections 3.1 and 3.2. Subsequently, the hydrodynamic results are presented in Sections 4.1, 4.2, and 4.3, while the finite element analysis results are shown in Section 4.4. Finally, Section 5 provides a summary of the results.

2 MATHEMATICAL MODEL

2.1 The basic principle of CFD-DEM coupling

In this paper, the propeller loads in crushed ices is calculated by the CFD-DEM coupling method. The phases in calculations involve fluid, solid and the fluid-solid interaction.

2.1.1 Fluid phase

The fluid is modeled as an incompressible Newtonian fluid. Ignoring the heat exchange between fluid and ice particles, the fluid motion satisfies the continuity equation and the momentum conservation equation, given as(Norouzi et al 2016),

$$\frac{\partial\left(\varepsilon_f \rho_f\right)}{\partial t}+\nabla\cdot\left(\varepsilon_f \rho_f \boldsymbol{u}\right)=0 \tag{1}$$

$$\begin{aligned}&\frac{\partial\left(\varepsilon_f \rho_f \boldsymbol{u}\right)}{\partial t}+\nabla\cdot\left(\varepsilon_f \rho_f \boldsymbol{u}\boldsymbol{u}\right)\\&=-\varepsilon_f \nabla P-\boldsymbol{F}+\nabla\cdot\left(\varepsilon_f \boldsymbol{\tau}_f\right)+\varepsilon_f \rho_f \boldsymbol{g}\end{aligned} \tag{2}$$

Where, ρ_f, P, τ_f and $\boldsymbol{g}$ are the fluid density, the time-average pressure, the viscous stress tensor and the gravitational acceleration, respectively. ε_f is the volume fraction of fluid in control volume. $\boldsymbol{F}$ is the average of resistance on ice particles in control volume.

2.1.2 Solid phase

For the solid phase, which means ice particles, the motion can be described by Newton's second law of motion, written as(He et al 2018),

$$m\frac{d\boldsymbol{v}}{dt}=\boldsymbol{F}_f+\boldsymbol{F}_c+m\boldsymbol{g} \tag{3}$$

$$I\frac{d\boldsymbol{\omega}}{dt} = \boldsymbol{T}_f + \boldsymbol{T}_c \tag{4}$$

Where, m, I, v and $\boldsymbol{\omega}$ represent respectively the mass, inertia, translational and rotational velocities of the particle. $\boldsymbol{F}_f$ and $\boldsymbol{T}_f$ arise from fluid-solid interaction. $\boldsymbol{F}_c$ and $\boldsymbol{T}_c$ arise from particle-particle interaction. $\boldsymbol{F}_c$ involves the normal contact force $\boldsymbol{F}_n$ and normal damping force $\boldsymbol{F}_{d,n}$, tangential contact force $\boldsymbol{F}_t$ and tangential damping force $\boldsymbol{F}_{t,n}$, while $\boldsymbol{T}_c$ is caused by these contact forces. The simulation of contact model between particles is based on Hertz-Mindlin contact theory(He et al 2015).

2.1.3 Fluid-solid coupling

Ice particles are regarded as viscoelastic particles. Hertz-Mindlin model is the commonly used contact model in DEM(Luo et al 2020). The model is a variant of a non-linear spring-damped contact model based on Hertz-Mindlin contact theory(Johnson 1985; Luo et al 2020).

The forces between two spheres are described by the equations:

$$\boldsymbol{F}_{contact} = F_n\mathbf{n} + F_t\mathbf{t} \tag{5}$$

In the formula, $\boldsymbol{F}_n$ is the normal force and $\boldsymbol{F}_t$ is the tangential force.

The normal force:

$$F_n = -K_n d_t - N_n v_t \tag{6}$$

In the formula:

$$K_n = \frac{4}{3}E_{eq}\sqrt{d_n R_{eq}} \tag{7}$$

$$N_n = \sqrt{\left(5K_n M_{eq}\right)}N_{ndamp} \tag{8}$$

$$N_{ndamp} = -\ln\left(C_{nrest}\right) / \sqrt{\pi^2 + \ln\left(C_{nrest}\right)^2} \tag{9}$$

The tangential force:

$$F_t = \begin{cases} -K_t d_t - N_t v_t \\ , \quad \left(\left|K_t d_t\right| < \left|K_n d_n\right| C_{fs}\right) \\ \left|K_n d_n\right| C_{fs} d_t / \left|d_t\right| \\ , \quad \left(\left|K_t d_t\right| > \left|K_n d_n\right| C_{fs}\right) \end{cases} \tag{10}$$

In the formula:

$$K_t = 8G_{eq}\sqrt{d_n R_{eq}} \tag{11}$$

$$N_t = \sqrt{\left(5K_t M_{eq}\right)}N_{tdamp} \tag{12}$$

$$N_{tdamp} = -\ln\left(C_{trest}\right) / \sqrt{\pi^2 + \ln\left(C_{trest}\right)^2} \tag{13}$$

here, K_n, K_t are normal spring stiffness and tangential spring stiffness. The N_n, N_{ndamp} are normal damping and normal damping coefficient. The N_t, N_{tdamp} are tangential damping and tangential damping coefficient. R_{eq}, M_{eq}, E_{eq} and G_{eq} is the equivalent radius, particle mass, Young's modulus, and shear modulus, respectively. d_n and d_t are overlaps in the normal and tangential directions at contact point. v_n and v_t are the normal and tangential velocity components of the relative sphere surface velocity at the contact point. C_{nrest} and C_{trest} are the normal and tangential coefficient of restitution. C_{fs} is the coefficient of friction between particles. For particle-wall collisions, the formulas are the same, but the wall radius and mass are assumed to be $R_{wall} = \infty$ and $M_{wall} = \infty$.

In this paper, the force $\boldsymbol{F}_f$, due to fluid-solid interaction, includes the drag force $\boldsymbol{F}_d$, pressure gradient force $\boldsymbol{F}_n$ (considering buoyancy effect) and virtual mass force $\boldsymbol{F}_a$.

The drag force is given as,

$$\boldsymbol{F}_d = \frac{1}{2}C_d \rho A_p \left|\boldsymbol{v}_s\right| \boldsymbol{v}_s \tag{14}$$

The drag force coefficient C_d is calculated based on Haider and Levenspiel drag coefficient(Haider & Levenspiel 1989), given as,

$$C_d = \frac{24}{\mathrm{Re}_p}\left(1 + A\,\mathrm{Re}_p{}^B\right) + \frac{C}{\left(1 + \frac{D}{\mathrm{Re}_p}\right)} \tag{15}$$

Where, $\boldsymbol{v}_s = \boldsymbol{u} - \boldsymbol{v}$, A_p is surface area of particle Re_p is the Reynolds number of particle. A, B, C and D are Coefficients related to the sphericity of particle.

The pressure gradient force $\boldsymbol{F}_p$ is given as,

$$\boldsymbol{F}_p = -V_p \nabla p_{static} \tag{16}$$

Where, V_p and ∇p_{static} are, respectively, the volume of the particle, static pressure gradient.

When particle undergoes acceleration in fluid, due to the inertia of fluid, the force acting on the particle is greater than its inertial force. The additional force is virtual mass force $\boldsymbol{F}_a$, given as,

$$\boldsymbol{F}_a = C_a \rho V_p \left(\frac{D\boldsymbol{v}_s}{D_t} - \frac{d\boldsymbol{v}}{d_t}\right) \tag{17}$$

Where, C_a is the virtual mass Coefficient, D/D_t is material derivative.

2.2 Basic equations of FEM

The strength analysis of propeller is conducted based on FEM. The equation of motion for the structural deformation of propeller is given as(Lee et al 2014),

$$\mathbf{M_S}\ddot{\mathbf{d}} + \mathbf{C_S}\dot{\mathbf{d}} + \mathbf{K_S}\mathbf{d} = \mathbf{F_{ST}} \tag{18}$$

Where, $\ddot{\mathbf{d}}$, $\dot{\mathbf{d}}$, $\mathbf{d}$ are acceleration, velocity, and displacement, respectively. $\mathbf{M_s}$ is mass matrix. $\mathbf{C_s}$ is damping matrix. $\mathbf{K_s}$ is stiffness matrix. $\mathbf{F_{st}}$ represents the total of all loads acting on the propeller, including the hydrodynamic loads $\mathbf{F_{fluid}}$, the contact force between the structure of propeller and crushed ice $\mathbf{F_{contact}}$, and centrifugal force $\mathbf{F_{ce}}$, Coriolis force $\mathbf{F_{co}}$.

2.3 Analysis procedure

Covering open and ducted type propellers with a fixed or controllable pitch, the IACS URI3 rules specify the ice loads. Ships navigating in ice-infested polar waters are assigned to seven polar classes, and strength requirements of structure gradually increase from class 7 to class 1. In each class, five cases and specific forces are stipulated, as shown in Table 1(IACS 2011).

Table 1 Ice loading conditions

Load case	Force	Loaded area	
1	F_b	area between 0.6R and 1.0R spanwise and from the L.E. to 20% chord chordwise	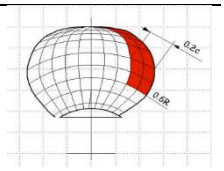
2	50% F_b	area between 0.9 and 1.0R in span and the whole chord	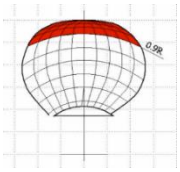
3	F_f	area between 0.6R and 1.0R spanwise and from the L.E. to 20% chord chordwise	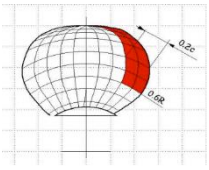
4	50% F_f	area between 0.9 and 1.0R in span and the whole chord	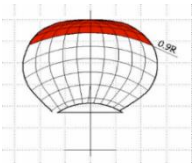
5	60% $MAX\{F_b, F_f\}$	area between 0.6R and 1.0R spanwise and from the L.E. to 20% chord chordwise	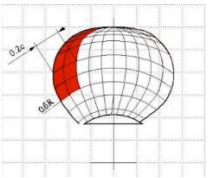

Where, R is the propeller radius and c is the chord length.

F_b is a force bending a propeller blade backwards and applied to an area on the back (suction) side of the blade as distributed loads in specific areas. F_f is a force bending a propeller blade forwards and applied to an area on the face (pressure) side of the blade as distributed loads in specific areas.

In case 1 and case 3, propeller operates in the first-quadrant, with ice milling on blade back (upstream) side enclosed and on blade face (downstream) side enclosed, respectively(Liu et al 2015).

In case 2 and case 4, propeller operates in the first-quadrant, ice block impacts on the blade back (upstream) side enclosed and on blade face (downstream) side enclosed, respectively.

In case 5, propeller operates in the third-quadrant, in reverse or astern motion with ice milling on the blade face (downstream) side enclosed.

In this paper, the working condition is assumed that when the ship is sailing, crushed ice flows along the hull towards the propeller and collides with the propeller suction surface, which is similar to case 2. According to case 2, the release zone of crushed ice is set as area covering 0.9 and 1.0R in span and the whole chord. Under the crushed ice-water flow, the superposition loads on the propeller is simulated and calculated by CFD-DEM method. Then, the stress distribution of the propeller is simulated and strength checking is conducted based on FEM method. The analysis procedure is shown in Figure 1.

In URI3, the specified minimum safety factor S_F of blade structure is greater than 1.5, given as,

$$S_F = \frac{\sigma_{ref}}{\sigma} \geq 1.5 \tag{19}$$

Where, σ is the calculated equivalent stress. σ_{ref}. $\sigma_{ref} = min\{0.7\sigma_u, 0.6\sigma_{0.2} + 0.4\sigma_u\}$. $\sigma_{0.2}$and σ_u are the proof stress at 0.2% strain and the ultimate tensile stress for the blade material, respectively.

3 CALCULATION MODELING

3.1 Ice-propeller-fluid model and relative parameters

The research object of this study the P1489R ice-class propeller, the detailed geometric parameters are shown in Table 2, and the three-dimensional model is shown in Figure 1. The material of propeller is Nickel–aluminum–bronze (NAB), and the material parameters are shown in Table 3(Liu et al 2015). According to the material parameters, the reference stress value σ_{ref} is 364MPa, as $0.7\sigma_u = 434$MPa and $0.4\sigma_u + 0.6\sigma_{0.2} = 364$MPa.

Table 2 Propeller geometric parameters

Parameter		Unit	Model-scale	Full-scale
diameter	D	m	0.22	3.19
Pitch ratio	$(P_{0.75R}/D)$	-	0.9	0.9
EAR	A_E/A_0	-	0.6	0.6
blade number	Z	-	4	4

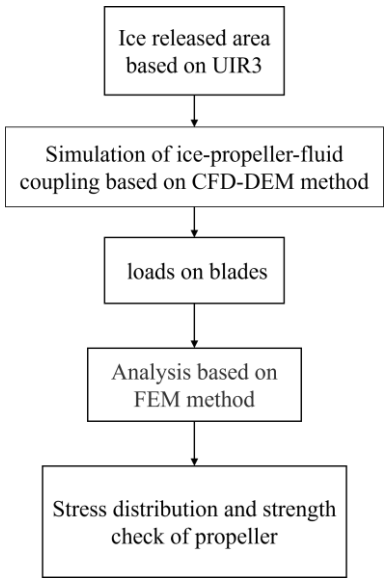

Figure 1 Analysis procedure

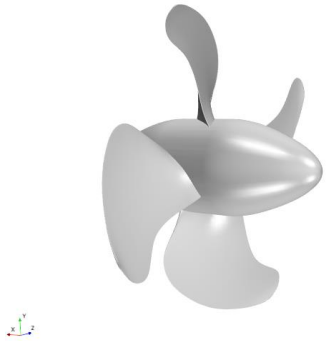

Figure 2 The propeller model

Table 3 The material parameters of NAB

Properties	Units	Value
Density ρ	kg/m^3	7600
Young's modulus E	GPa	117.6
Poisson ratio υ	-	0.34
Yield	MPa	268.9
Ultimate tensile	MPa - σ_u	620.53
Proof stress	MPa - $\sigma_{0.2}$	193.05

The numerical simulation of ice-propeller-fluid interaction is conducted using an overlapping grid method. The computational region consists of a rotation region and a static region, which is shown as Figure 3. Trimmed cell mesh is generated, and the total number of mesh cell is 3945977, which is shown as Figure 4.

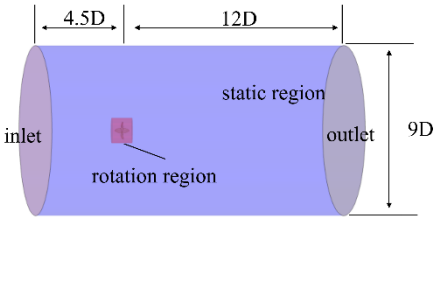

Figure 3 The computational region

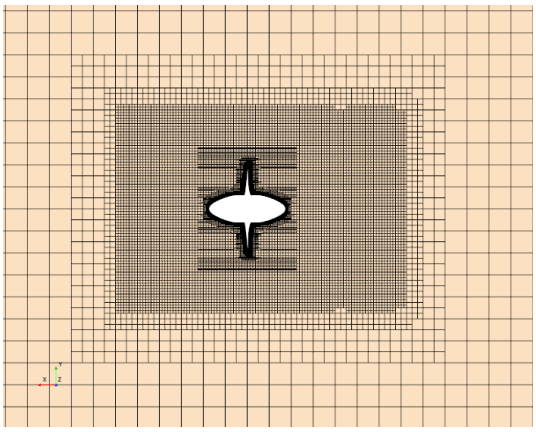

Figure 4 The generated mesh

Ice particles are simulated by the DEM particles, and combining small spherical particles can form the desired non-spherical or irregular shape models. In the marginal ice zone of the Antarctic region, there are mass of new ice types including frazil, nilas, brash, and pancake ice. Including the ridged ice which has much higher thickness, the mean level ice thicknesses are approximately 10 cm(Xie et al 2011). Considering that the thicknesses of amounts of ice are less than 10cm, we take the thickness of particles as 7.25cm in full-scale model in this manuscript. To simplify the calculations, a basic spherical particle model is used to simulate crushed ices, with a particle diameter of 0.005m. The parameters related to the ice material are shown in Table 4(Sorsim et al 2016; Timco & Weeks 2010). The ice particles are injected by the injector defined in front of the propeller, with the distance between the injector and the propeller being D. The injector particle arrangement is 4*30, and according to URI3, the injector covers the area between 0.9 and 1.0R in span and the whole chord. The area selected is dangerous and easy to impact with ice particles.

DEM particles are Lagrange particles that enter the continuous liquid phase and interact with the fluid. When the DEM particle is smaller than the fluid grid, the influence of the particle as the mass source and momentum source can be completely transferred to the fluid grid. When the DEM particle is larger than the fluid grid, the fluid grid will be covered by DEM particle, and the numerical instability will occur. To solve this problem, it is necessary to set the grid cell cluster in Star-CCM+, generate rough mesh, and set its approximate scale to be

larger than the DEM particle scale.

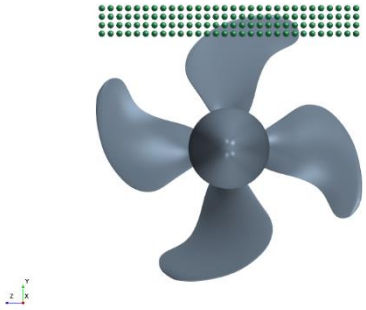

Figure 5 The propeller and injector

Table 4 The ice material parameters

Parameter	Unit	Value
Density ρ	kg/m^3	920
Young's modulus E	GPa	2.7
Poisson ratio υ	-	0.35

The interaction between ice particles and fluid is simulated by two-way coupling, where the flow acts on the ice particles, affecting their trajectories, and the motion of the particles reacts on the fluid. The particle physics model selects two-way coupling DEM particles, drag force, pressure gradient force, and virtual mass. The physical model for CFD calculations includes coupled flow, gravity, discrete element model (DEM), and multi-phase interaction, etc. The relevant parameters for the interactions between ice particles and ice particles - wall are shown in Table 5(Sorsimo et al 2016). The velocity of the particles is consistent with the flow velocity, with a velocity rate of 9600/s, keeping the ice concentration along the axis of propeller closed to 20%. A pressure-based coupled solver is used with the Coupled algorithm. Shear stress transport SST $k-\omega$ model is selected for the turbulence model, and the numerical calculation time step is less than the time required when the propeller rotates 1° (propeller speed n = 600 r/ min), which is 2.5×10^{-4}s.

Table 5 The ice material parameter

objects	Properties	Value
Particles-particles	μ_r	0.5
	μ_n	0.8
	μ_t	0.8
Particles-wall (propeller)	μ_r	0.05
	μ_n	0.6
	μ_t	0.6

Dimensional analysis of the propeller thrust T and torque Q is performed as follows:

$$J = \frac{V_A}{nD} \tag{20}$$

$$KT = \frac{T}{\rho n^2 D^4} \tag{21}$$

$$KQ = \frac{Q}{\rho n^2 D^5} \tag{22}$$

$$\eta = \frac{KT}{KQ} \cdot \frac{J}{2\pi} \tag{23}$$

Where, ρ is the density of fluid. D is the diameter of propeller. n is the rotate speed of propeller. KT, KQ are thrust coefficient, torque coefficient, respectively. η is propulsive efficiency.

3.2 Finite element models

Take the propeller blade, use the method of tetrahedrons to mesh it, and apply the typical pressure distribution along the radius under different working conditions to the blade, fixing the contact end with the propeller hub, to obtain the stress and strain distribution of the blade. Before the blade stress analysis is carried out, the blade mesh is firstly analyzed for grid independence, the base size of the mesh is changed, and the change rate of peak stress is analyzed by applying the same loads. Secondly, since the pressure is applied to the propeller blade in the form of a strip along the radius, it is also necessary to consider the influence of the number of strips on the stress, and select an appropriate number of strips. In finite element analysis, the mesh model is shown in Figure 6, while pressure is applied on blade when the strips divided are three.

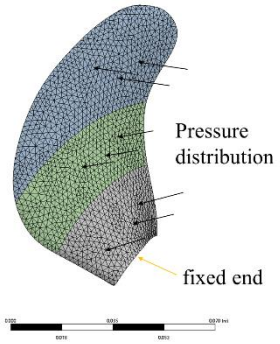

Figure 6 The finite element model of blade

4 RESULTS, ANALYSIS and DISCUSSION

4.1 Hydrodynamic characteristic of propeller in open water

Before conducting numerical simulation of ice-propeller-fluid interaction, the hydrodynamic performance of the propeller in open water is calculated with a range of the advance coefficients (J) from 0.1 to 0.7. Three type of grid densities of flow field are set, in which the base mesh sizes are increased progressively by a factor of $r_k = \sqrt{2}$. The results are shown as Figure 7. The simulations are conducted using the fine grids, with the hydrodynamic performance in open water shown in Table 6.

In order to investigate the hydrodynamic performance and force of propeller, the advance coefficients range of 0.4~0.6 is selected to investigate the influence of crushed ice flowing to the suction surface on the force and strength

of the propeller. Then, due to the maximum thrust on the blade under bollard conditions, the propeller force and strength problems are also studied.

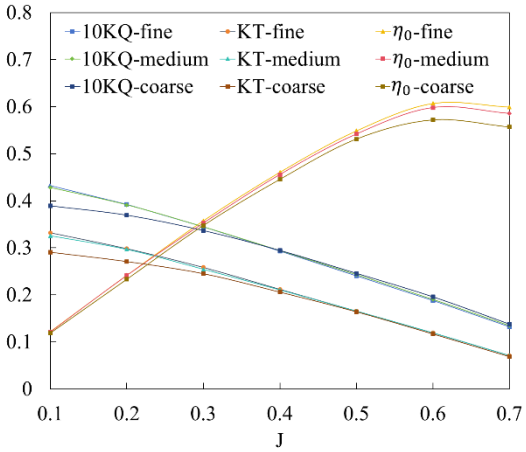

Figure 7 The open water performance at different grid densities

Table 6 The hydrodynamic performance in open water

J	0.1	0.2	0.3	0.4	0.5	0.6	0.7
KT	0.3322	0.2984	0.2586	0.212	0.1658	0.1196	0.0714
10KQ	0.4321	0.3924	0.3451	0.2928	0.2404	0.1881	0.1326

4.2 Hydrodynamic characteristic of propeller in ice condition when J=0.4~0.6

In the simulation of propeller in ice flow, the propeller works in open water to reach convergence and the time range ranges from 0 to 0.3s in the first stage. Then, the ice particles are released between 0.3~0.42s, to form a part of channel containing amounts of ice particles. The ice particles are affected by the flow filed of propeller, and disturb the flow field. Some ice particles collide with propeller. To investigate the behavior of ice particles, take the numerical calculation of ice-propeller-fluid under the case J=0.6 as example.

The motion states of crushed ice particles at different moments are shown in Figure 8. It can be seen that as the ice particles approaching to propeller, the speeds show an increasing trend, which are affected by the suction effect of the propeller. When the particles flow through the propeller area, some particles collide with the propeller, the speeds of which increase and the trajectories of which change. Under the indirect influence of the fluid medium and the direct influence of ice-propeller collision, the ice particles become disorderly and some move towards the center of the propeller axis.

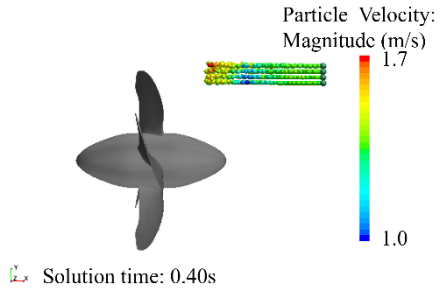

(a1) Side view of velocity distribution at 0.4s

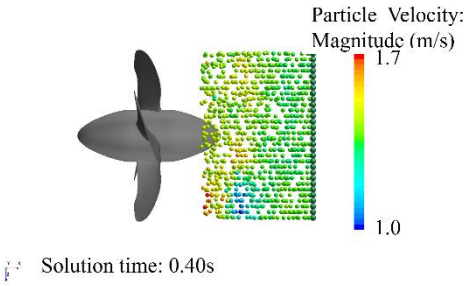

(a2) Top view of velocity distribution at 0.4s

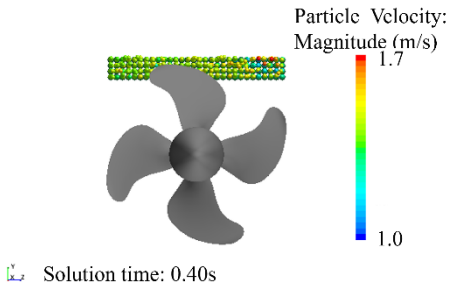

(a3) Front view of velocity distribution at 0.4s

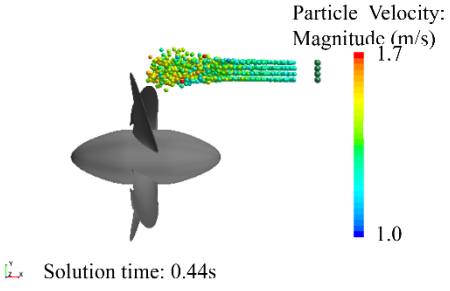

(b1) Side view of velocity distribution at 0.44s

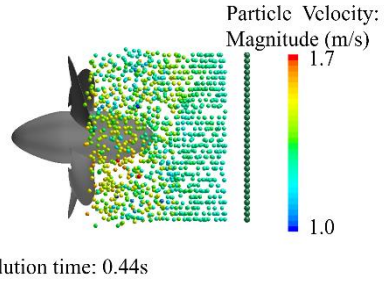

(b2) Top view of velocity distribution at 0.44s

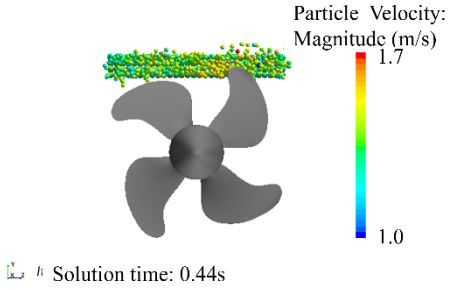

(b3) Front view of velocity distribution at 0.44s

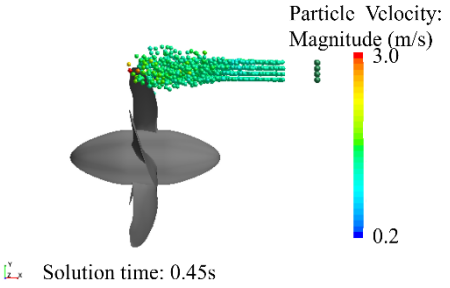

(c1) Side view of velocity distribution at 0.45s

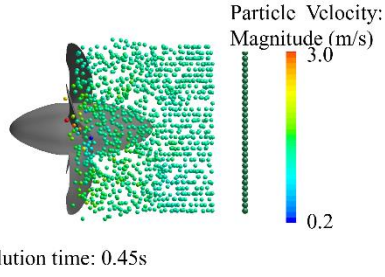

(c2) Top view of velocity distribution at 0.45s

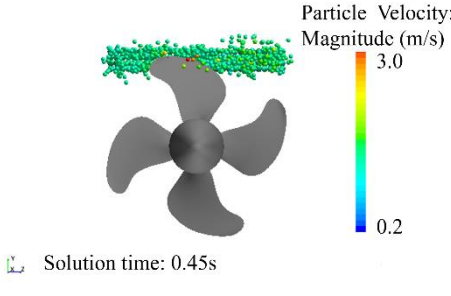

(c3) Front view of velocity distribution at 0.45s

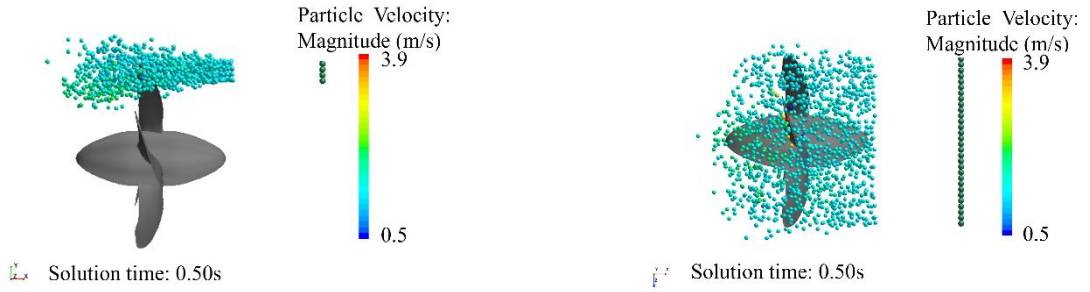

(d1) Side view of velocity distribution at 0.5s **(d2) Top view of velocity distribution at 0.5s**

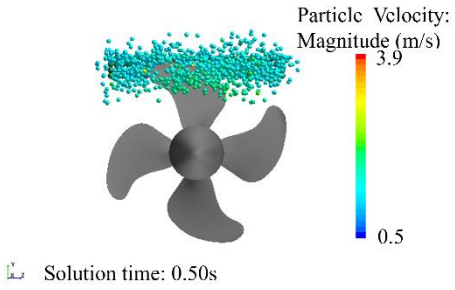

(d3) Front view of velocity distribution at 0.5s

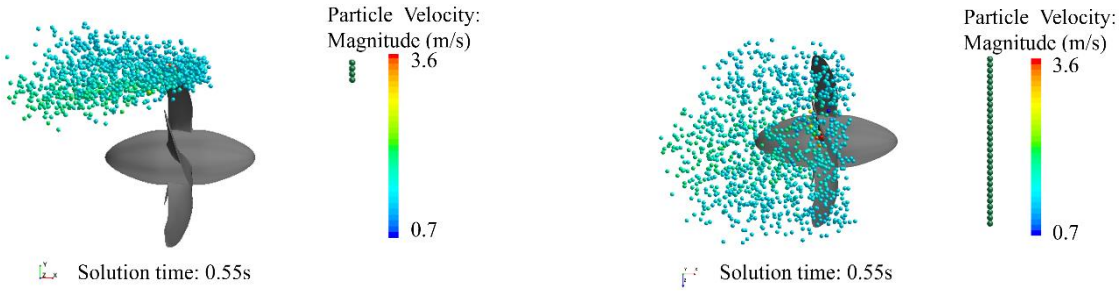

(f1) Side view of velocity distribution at 0.55s **(f2) Top view of velocity distribution at 0.55s**

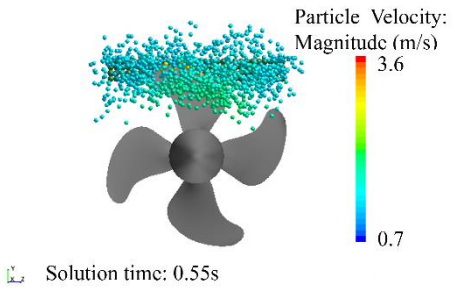

(f3) Front view of velocity distribution at 0.55s

Figure 8 The movement states of crushed ices over time in J=0.6

The dimensionless numbers that characterize propeller propulsive performance in condition J=0.6, KT and KQ, are shown in Figure 9. Compared with Figure 8, the influence of the propeller is relatively small during the initial stage of particle release. As the particles approach and contact with the propeller, KT and KQ experience significant fluctuations. When the advance coefficients are 0.4 and 0.5, the hydrodynamic performance of the propeller are shown in Figure 10. The average values of KT and KQ during the interaction between the propeller and ice particles are taken and compared with the results under open water conditions, as shown in Table 7. In ice-fluid

flow, the propulsive efficiency of the propeller is lower than that in open water, mainly due to the increase of torque coefficient. Moreover, as the advance coefficient increases, the propulsive efficiency reduction increases.

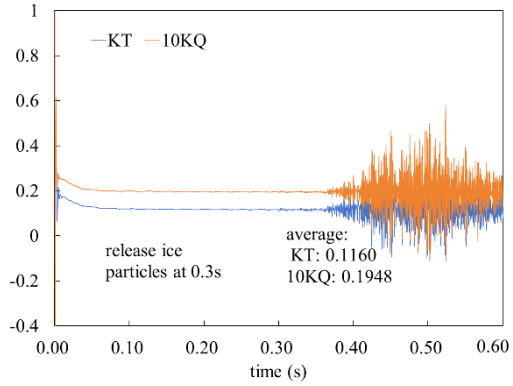

Figure 9 Hydrodynamic performance (J=0.6)

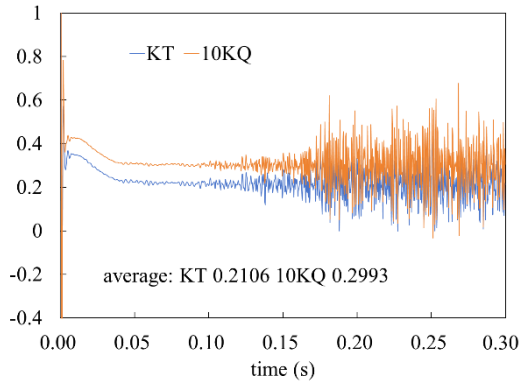

(a) J=0.4

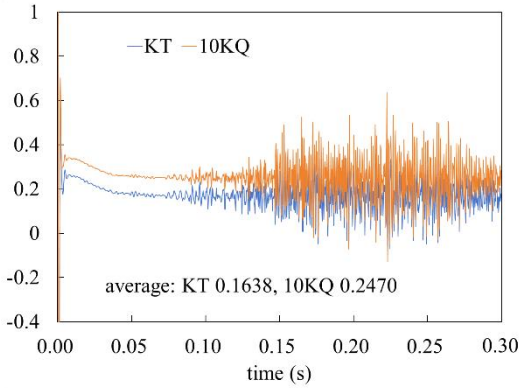

(b) J=0.5

Figure 10 Hydrodynamic performance (J=0.4 and J=0.5)

Table 7 The comparation of hydrodynamic performance in open water and ice flow

J	$10KQ_{o\_w}$	$10KQ_{ice}$	$10KT_{o\_w}$	KT_{ice}	η_{o_w}	η_{ice}	$\lvert(\eta_{ice}-\eta_{o\_w})/\eta_{o\_w}\rvert$
0.4	0.2928	0.2993	0.212	0.2106	0.4609	0.4479	2.8%
0.5	0.2404	0.2470	0.1658	0.1638	0.5488	0.5277	3.85%
0.6	0.1881	0.1948	0.1196	0.1160	0.6072	0.5686	6.35%

The propeller rotation speed is 10rps, and the thrust and torque of the propeller during the period t ~ t+0.05 s under different advance coefficients are taken, as shown in Figure 11. During this period, the propeller rotates half a circle, and the two blades rotate through the particle region. The motion states of the blades at typical time nodes are shown in Figure 12. Comparing Figure 11 and Figure 12, it can be seen that when the blade is directly facing the ice particle release area, the fluctuation amplitude of the thrust and torque acting on the propeller is the largest, and the force acting on the propeller presents periodic changes.

The Fourier transform of the propeller thrust and torque is shown in Figure 13. With the increase of the advance coefficient, the thrust and torque of the propeller decrease, while the fluctuation frequencies of the thrust and torque increase.

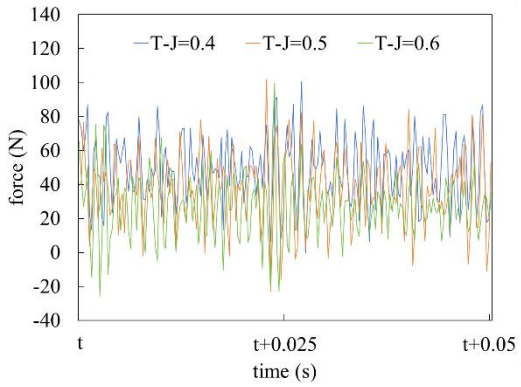

(a) The thrust during t ~ t+0.05s

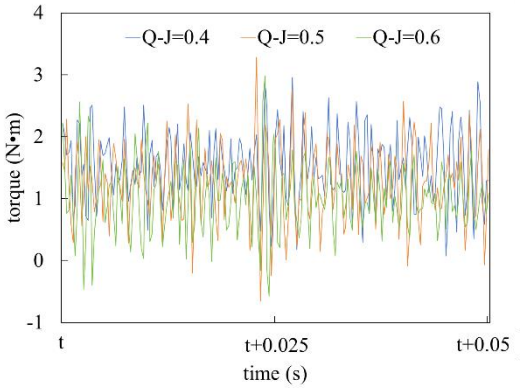

(b) The torque during t ~ t+0.05s

Figure 11 The thrust and torque of propeller

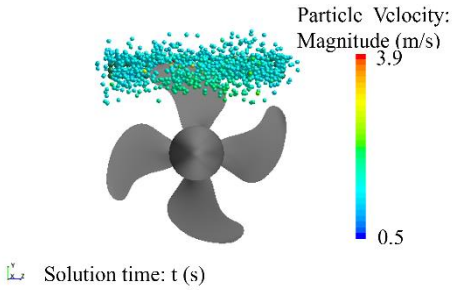

(a) The motion state at t s

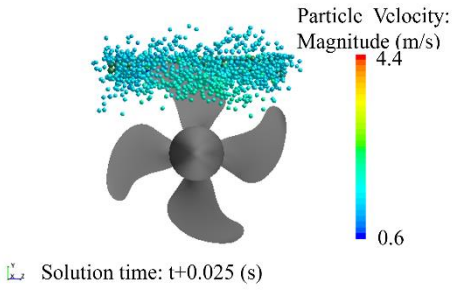

(b) The motion state at t+0.025 s

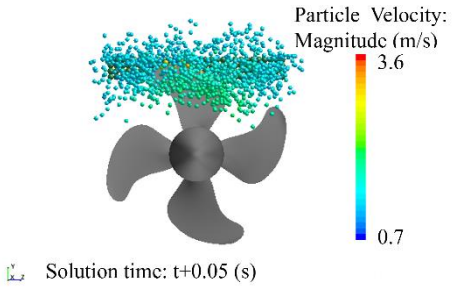

(c) The motion state at t+0.05 s

Figure 12 Motion states of propeller and particle under selected time nodes (J=0.6)

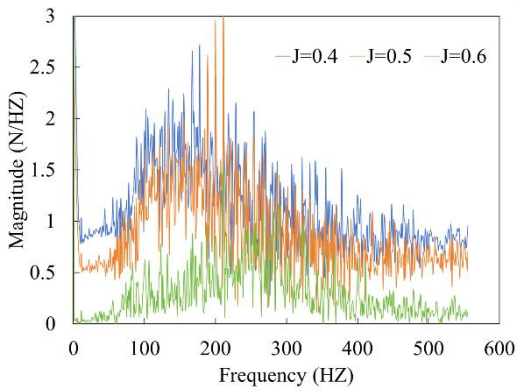

(a) Fourier transformation of thrust

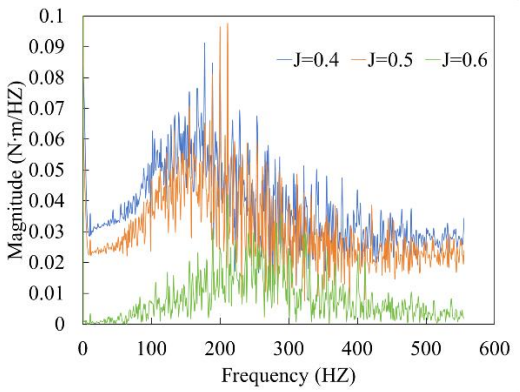

(b) Fourier transformation of torque

Figure 13 Fourier transformation of thrust and torque of propeller

The pressure time history curves of blade tip at different radiuses under the condition J = 0.6 are extracted, as shown in Figure 14. Before the releasing of particles, the pressure at each radius is in a relatively stable pulsating state, and

the absolute value of the pressure decreases first and then increases along the radius, with the maximum pressure at the blade tip. In ice particle flow, the pressure at each radius fluctuates sharply, and the direction of the fluctuation has a certain synchronization, and the peak value appears at the tip of the blade.

The pressure time history curves at the tip of the blade under different advance coefficients are taken, as shown in Figure 15. When the ice particles are released at same time, the pressure fluctuation of the blade tip occurs faster under the high advance coefficient, and the value of fluctuation peak is greater.

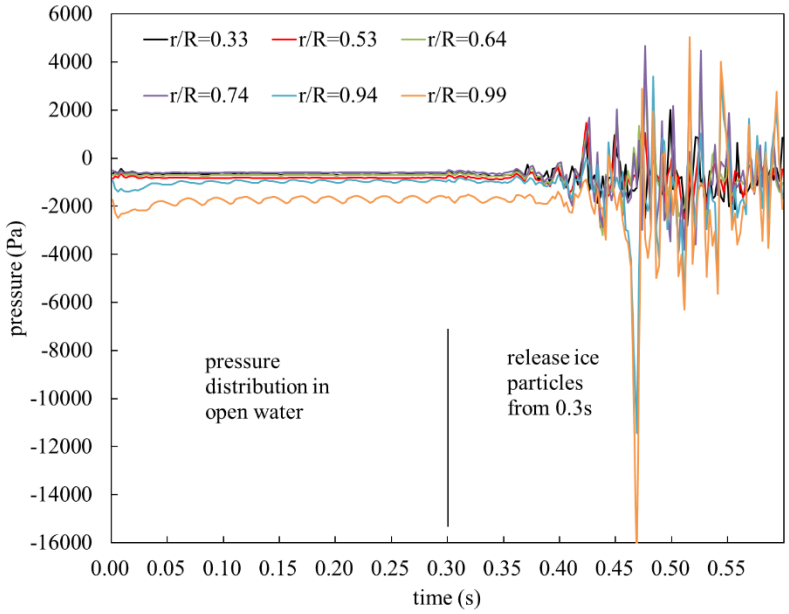

Figure 14 The pressure distribution along the radius (J=0.6)

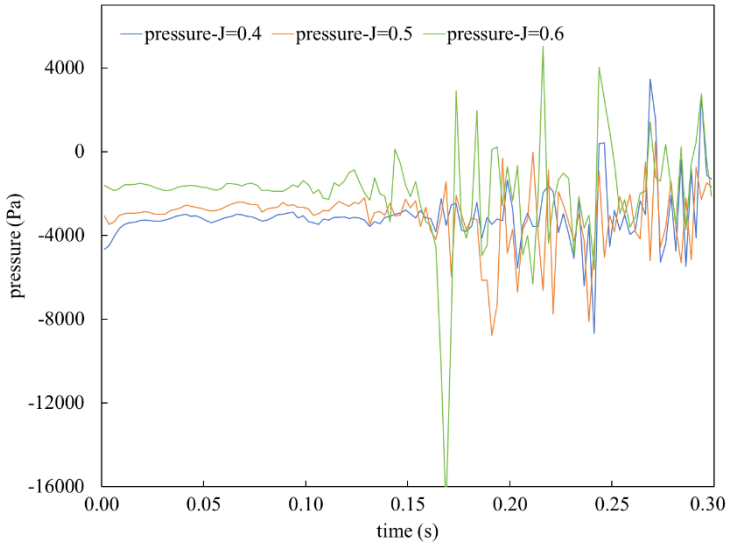

Figure 15 The pressure time histories of blade tip

4.3 Hydrodynamic characteristic of propeller in ice condition when J=0

In open water, the propeller experiences the maximum thrust and torque under bollard condition). In this paper, the propeller in open water and ice flow under bollard conditions are numerically simulated respectively. As the initial velocity of ice particle is set as 0 m/s, the injector is changed which releases the ice particles at the same time, and the number and concentration of ice particles are consistent with conditions above.

In the first stage, the simulation is conducted in open water from 0~0.2s to reach the convergence. Then, the ice particles enter the fluid flow, and move under the suction of propeller. The states of motion are shown in Figure 16. Under the effect of suction of propeller, the ice particles approach the propeller with speeds increasing. Some ice particles collide with propeller, and the leading edge of propeller is the most vulnerable area for collisions. The speeds of ice particles which collide with blades increase rapidly, and decrease under the influence of fluid.

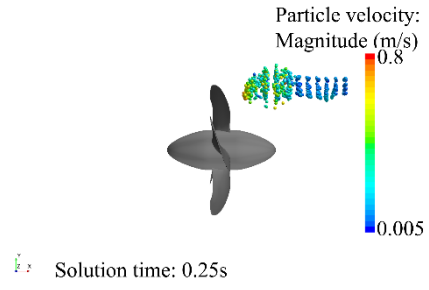

(a1) Side view (velocity distribution at 0.25s)

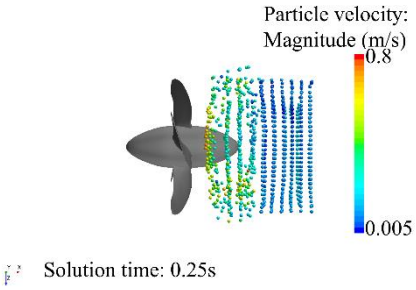

(a2) Top view (velocity distribution at 0.25s)

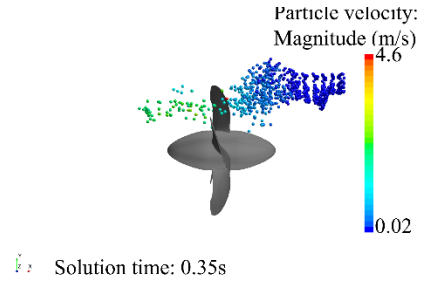

(b1) Side view (velocity distribution at 0.35s)

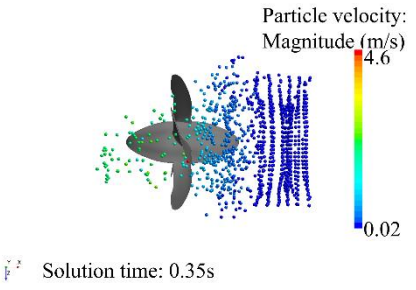

(b2) Top view (velocity distribution at 0.35s)

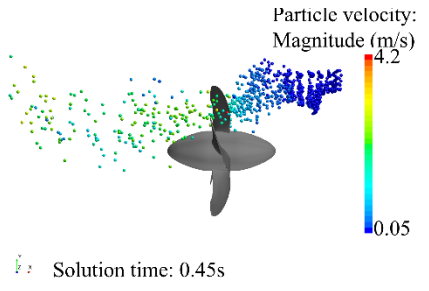

(c1) Side view (velocity distribution at 0.45s)

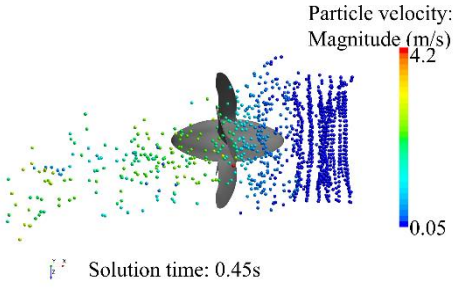

(c2) Top view (velocity distribution at 0.45s)

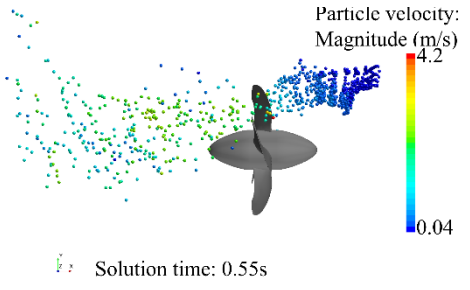

(d1) Side view (velocity distribution at 0.55s)

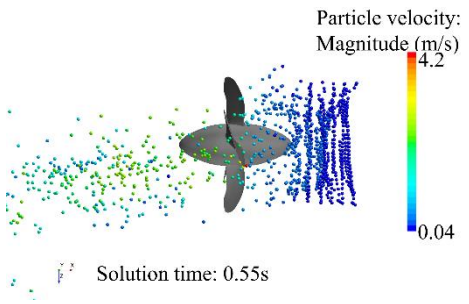

(d2) Top view (velocity distribution at 0.55s)

Figure 16 The movement states of crushed ices over time in J=0

The thrust and torque of the propeller in ice flow in J=0 are taken, as shown in Figure 17. The thrust and torque of propeller show periodicity. When the blade is close to the ice area, the fluctuations of thrust and torque are lager. Taking the mean values, the thrusts in crushed ice flow and in open water are 85.87 N and 85.21 N. The torques in crushed ice flow and in open water are 2.41 N and 2.39 N. Under the light ice conditions in this manuscript, the mean forces change a little in J=0.

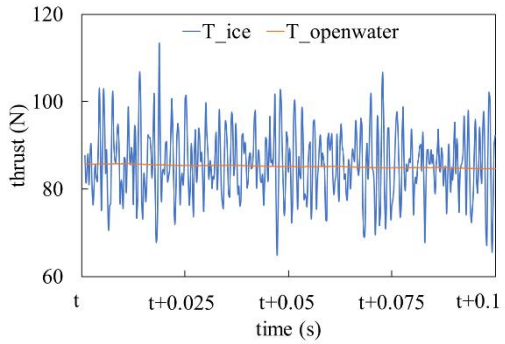

(a) Thrust of propeller

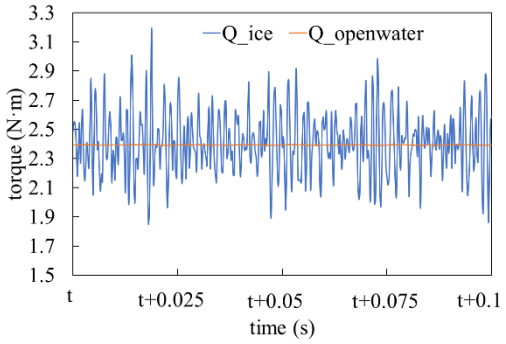

(b) Torque of propeller

Figure 17 The thrust and torque on propeller during 4 rotation periods of blades

The pressure time histories of the propeller blade along the radial direction during contacting with ice particles when J=0 are taken, as shown in Figure 18. It can be seen that multiple pressure peak and valley values of radial direction show approximate synchrony. The pressure changes near the tip of the blade in the crushed ice flow and of the blade in open water are taken, as shown in Figure 19. The pressure on the tip of the blade is greatly increased in ice flow.

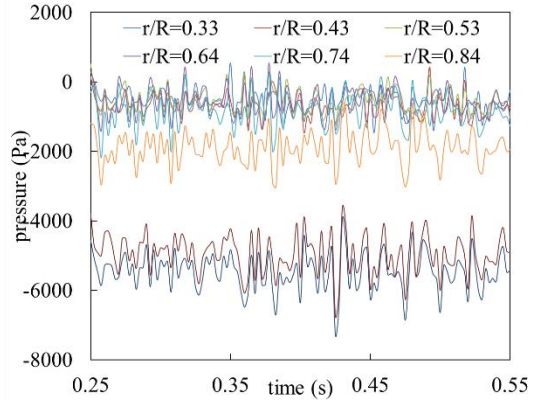

Figure 18 The pressure distribution along radius of blade during two rotation periods of propeller

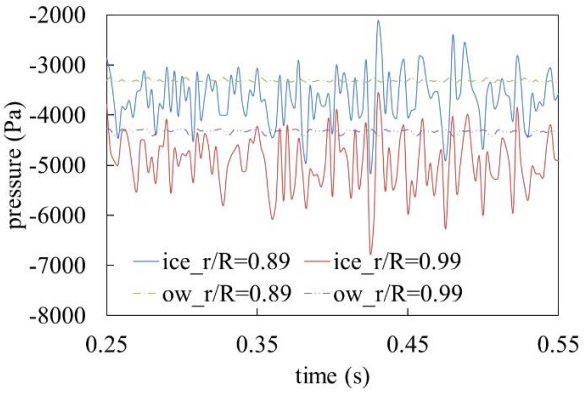

Figure 19 The comparation of pressure on blade in open water and ice fluid during two rotation periods of propeller (ice_r/R means the radial position in ice flow, ow_r/R means the radial position in open water)

4.4 The strength analysis of propeller

In order to investigate the strength of the propeller, the maximum pressure distributions under the ice–propeller–fluid interaction, are applied to the blade along the radial direction to study the stress distribution.

When J=0.6, the radial pressure on the blade in ice flow is taken, and the pressure at the peak point in Figure 14 is applied to the finite element model of blade in the manner shown in Figure 6. The grid density of the blade finite element model changed, as shown in Table 8, which includes case1~case4, and the maximum stress value is obtained, the mesh independence analysis is carried out. With the mesh refinement, the difference of maximum stress value between cases decreases, and the maximum stress value of case 4 is changed by 0.7% compared to case 3. The grid density of case 3 is subsequently used for calculation.

Table 8 Comparation of stress in cases with different grid density

case	Element numbers	Cell numbers	The maximum stress (MPa)	
1	4994	2594	11.762	
2	9439	5178	11.983	1.9%
3	26773	15872	12.159	1.5%
4	70149	44204	12.244	0.7%

The blade is divided into several strips for applying loads along the radial direction, as shown in Table 9, with three cases: case a, case b, and case c. Radial pressure from CFD model of blade in ice flow when J=0.6 is applied to the finite element model of blade. The maximum stress value of case c is changed by 0.2% compared to case b. Subsequent calculations are performed by applying pressure in this way (case b).

Table 9 Comparation of stress in cases with different strips divided

case	The number of loaded strips	The maximum stress (MPa)

a	3	12.159	
b	7	15.512	27.5%
c	11	15.544	0.2%

The stress and strain cloud diagrams of the blade in the ice flow with J=0.6 are shown in Figure 20 and Figure 21, respectively. The regions with large blade forces are distributed near the blade tip of the trailing edge and the leading edge, and the peak point appears in the trailing edge part. Figure 22 and Figure 23 respectively show the stress cloud diagram and strain cloud diagram of the blade stress in ice flow when J=0, and the stress peak value is 8.199MPa. Figure 24 and Figure 25 respectively show the stress cloud diagram and strain cloud diagram of the blade stress in open water when J=0, and the stress peak value is 5.325MPa.

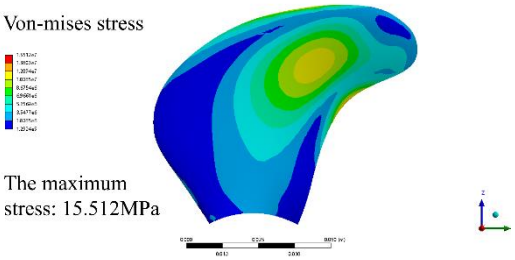

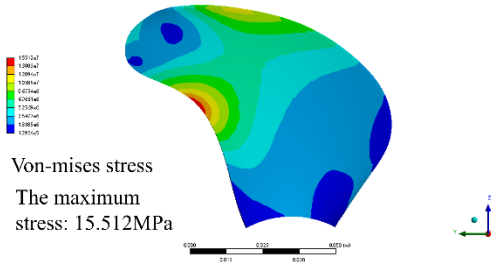

(a) The stress distribution of suction side **(b) The stress distribution of pressure side**

Figure 20 The stress distribution of blade in ice flow (J=0.6)

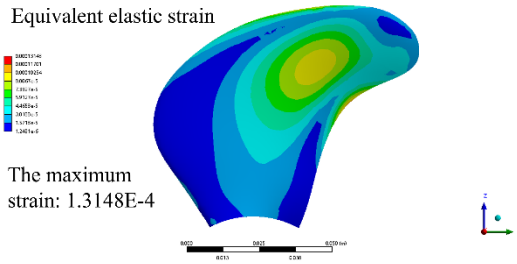

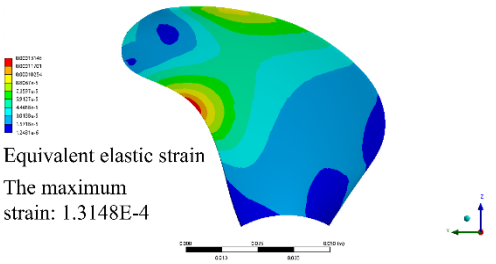

(a) The strain distribution of suction side **(b) The strain distribution of pressure side**

Figure 21 The strain distribution of blade in ice flow (J=0.6)

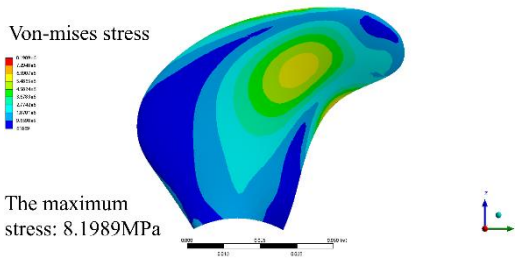

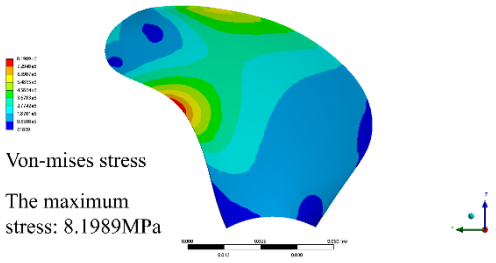

(a) The stress distribution of suction side **(b) The stress distribution of pressure side**

Figure 22 The stress distribution of blade in ice flow (J=0)

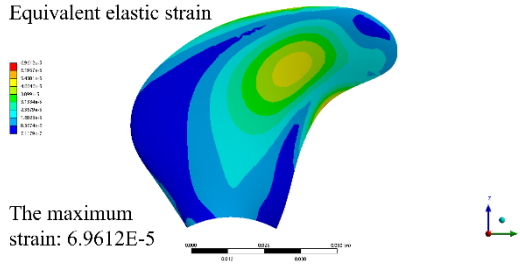

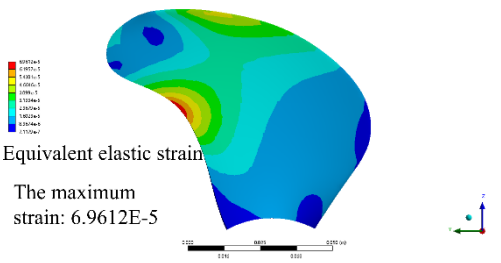

(a) The strain distribution of suction side **(b) The strain distribution of pressure side**

Figure 23 The strain distribution of blade in ice flow (J=0)

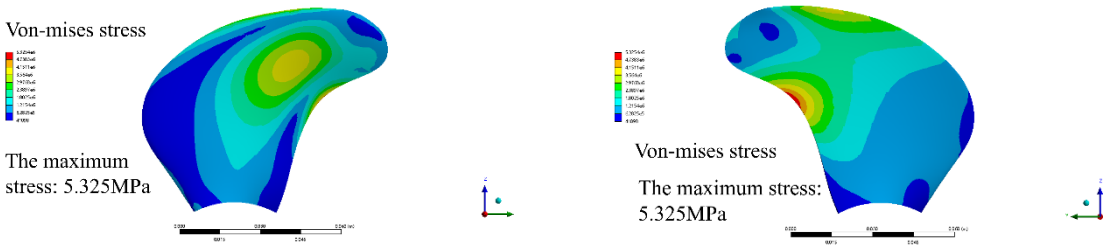

(a) The stress distribution of suction side **(b) The stress distribution of pressure side**

Figure 24 The stress distribution of blade in open water (J=0)

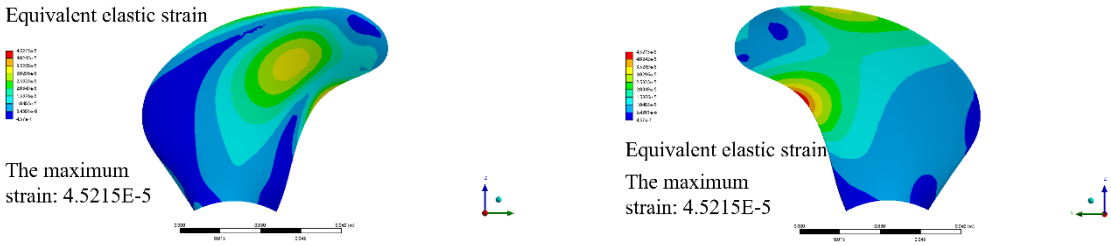

(a) The strain distribution of suction side **(b) The strain distribution of pressure side**

Figure 25 The strain distribution of blade in open water (J=0)

The safety factor of blade under different conditions are calculated, with σ_{ref}=364MPa. When J=0.6, in ice flow, $S_{F1}=\sigma_{ref}/\sigma$=364/15.512=23.5 . When J=0, in ice flow, $S_{F2}=\sigma_{ref}/\sigma$=364/8.1986=44.4 , and in open water, $S_{F3}=\sigma_{ref}/\sigma$=364/5.325=68.3. In the numerical simulations in this paper, the diameter and velocity of the ice particles selected are small, and the influence of ice on the propeller mainly comes from the disturbances of the flow field, so the calculated safety factor is large. At the high advance coefficient, the larger peak force points on blades are more likely to occur.

In the light ice conditions set in this manuscript, the hydrodynamic performances of propeller are affected, with propulsive efficiency decreasing. As the thickness of ice is thin, the collisions between ice particles and propeller cause no serious threat to the strength of the propeller.

When some particles collide with propeller, the states of the ice particles change rapidly, but the crushing of ice is not considered. From the perspective of energy dissipation, part of the kinetic energy ΔE_S is consumed via multiple means associated with ice, and the crushing process of is one of them, as(Li & Huang, 2022)

$$\Delta E_S = E_k + E_p + E_f + E_c + E_d \tag{24}$$

E_k, E_p, E_f, E_c, and E_d correspond to the modelling of ice motion, submerging, friction, crushing, and deformation (including cracking). The importance of each part varies depending on the type and size of ice. When studying the interactions between structures and crushed ice, which is small, crushed ice is regarded as unbreakable in many researches. However, there is no quantified criterion for justifying whether ice crushing could be ignored. Considering the ice particles are small and conservative estimates are acceptable for strength check, we think that ice is unbreakable at this stage. In further study, the factors, including the shape, size distribution and failure of ice, would be considered carefully and investigated.

5 CONCLUSIONS

In this paper, the method of blade strength analysis in ice flow is studied. Considering that crushed ice particles approach to the propeller along the bottom of the ship, the ice-propeller-fluid interaction is simulated based on CFD-DEM method to study the influence on the propeller hydrodynamic performance, obtain the pressure on the blade, and analyze the blade strength with FEM method.

In crushed ice flow, the pressure surface of the propeller near the leading edge is easy to collide with ice particles. The crushed ice particles set in this paper are small in diameter and number, and only a small part of the ice particles collide with the propeller. The hydrodynamic performance parameters, thrust coefficient, torque coefficient and propulsive efficiency of propeller are all affected by the indirect influence of particle disturbing flow field and the direct influence of particle contact with propeller. The thrust coefficient decreases, the torque coefficient increases, and the latter changes more greatly, and the propulsive efficiency decreases. With the increase of the advance coefficient, the decrease in propulsive efficiency increases. When a blade is facing the ice releasing area, the thrust and torque on the propeller are larger, and the thrust and torque show periodic characteristics. The frequency of thrust and torque fluctuation of propeller increases with the increase of

advance speed coefficient, providing a reference for considering propeller excitation force.

Through finite element analysis, the safety factors obtained are 44.4 and 23.5 under the conditions of 0 and 0.6 advance coefficients, respectively. The diameter and velocity of the ice particles selected in this paper are small, and the influence of ice on the propeller mainly comes from the disturbance of the flow field, so the calculated safety factor is large. Although the average pressure and torque under bollard conditions are larger, the maximum force peak points are more likely to occur under ice-propeller-flow interaction under high advance coefficient.

The research method in this paper can provide reference for the hydrodynamic performance analysis and strength check of propeller. Properties such as the change of size, velocity and shape of the ice particle, as well as the precision of the pressure applied, can then be further studied.

REFERENCES

Browne, R. P. (1997). Analysis of Canadian full scale propeller and ice interaction trials data for correlation with empirical models. National Research Council of Canada, Institute for Marine Dynamics, St. John's, Newfoundland, Canada.

Chen, Z., He, Y., Gu, Y., Su, B., Ren, Y., & Liu, Y. (2021). A novel method for numerical simulation of the interaction between level ice and marine structures. Journal of Marine Science and Technology, 26(4), 1170-1183.

Chunyu, G. U. O., Kang, H. A. N., Chao, W. A. N. G., Liyu, Y. E., & Zeping, W. A. N. G. (2022). Numerical modelling of the dynamic ice-milling process and structural response of a propeller blade profile with state-based peridynamics. Ocean Engineering, 264, 112457.

Guo, C.-y., Zhang, Z.-t., Tian, T.-p., Li, X.-y., & Zhao, D.-g. (2018). Numerical Simulation on the Resistance Performance of Ice-Going Container Ship Under Brash Ice Conditions. China Ocean Engineering, 32(5), 546-556.

Guo, C., Han, K., Wang, C., Ye, L., & Wang, C. (2021). Evaluation and analysis of the static strength of ice-class propellers. Ocean Engineering, 235, 109336.

Haider, A., & Levenspiel, O. (1989). Drag coefficient and terminal velocity of spherical and nonspherical particles. Powder Technology, 58(1), 63-70.

He, Y., Bayly, A. E., & Hassanpour, A. (2018). Coupling CFD-DEM with dynamic meshing: A new approach for fluid-structure interaction in particle-fluid flows. Powder Technology, 325, 620-631.

He, Y., Wang, Z., Evans, T. J., Yu, A. B., & Yang, R. Y. (2015). DEM study of the mechanical strength of iron ore compacts. International Journal of Mineral Processing, 142, 73-81.

Heydari, M., Sadat, H., & Nasrazadani, S. (2019). CFD-DEM-MBD Coupling to Study Ice Impacts on Propellers in Arctic Regions. Sixth International Symposium on Marine Propulsors smp'19, Rome, Italy.

IACS. (2011). Requirements Concerning Polar Class. International Association of Classification Societies, London.

Janßen, C. F., Mierke, D., & Rung, T. (2017). On the development of an efficient numerical ice tank for the simulation of fluid-ship-rigid-ice interactions on graphics processing units. Computers & Fluids, 155, 22-32.

Johnson, K. L. (1985). Contact Mechanics. Cambridge: Cambridge University Press.

Kang, H., Kaiqiang, W., Chunyu, G., Chao, W., Liyu, Y., & Zeping, W. (2023). Mechanism analysis of propeller-ice contact and rapid prediction of ice loads. Cold Regions Science and Technology, 216, 103987.

Lee, H., Song, M.-C., Suh, J.-C., & Chang, B.-J. (2014). Hydro-elastic analysis of marine propellers based on a BEM-FEM coupled FSI algorithm. International Journal of Naval Architecture and Ocean Engineering, 6(3), 562-577.

Li, F., & Huang, L. (2022). A Review of Computational Simulation Methods for a Ship Advancing in Broken Ice. Journal of Marine Science and Engineering, 10(2).

Liu, P., Bose, N., & Veitch, B. (2015). Evaluation, design and optimization for strength and integrity of polar class propellers. Cold Regions Science and Technology, 113, 31-39.

Luo, W., Jiang, D., Wu, T., Guo, C., Wang, C., Deng, R., & Dai, S. (2020). Numerical simulation of an ice-strengthened bulk carrier in brash ice channel. Ocean Engineering, 196, 106830.

Newburry, S., Browne, R. P., & Jones, S. J. (1994). Experimental Determination of Hydrodynamic Non-Contact Loads During Propeller/Ice Interaction. The Fourth International Offshore and Polar Engineering Conference, Osaka, Japan.

Newbury, S., Shih, L. Y., Browne, R. P., Revill, C. R., Kenny, S., & Zheng, Y. (1993). Experimental and theoretical evaluation of hydrodynamic pressure during non-contact propeller/ice interaction. 2nd Canadian Marine Dynamics Conference, Vancouver, British Columbia, Canada.

Norouzi, H., Zarghami, R., Sotudeh-Gharebagh, R., & Mostoufi, N. (2016). Coupled CFD-DEM modeling: formulation, implementation and application to multiphase flows. Chichester, UK ; Hoboken, NJ : John Wiley & Sons.

Searle, S., Veitch, B., & Bose, N. (2001). Experimental Investigation of a Highly Skewed Propeller in Ice. Journal of Offshore Mechanics and Arctic Engineering, 123(4), 191-197.

Shen, H. T., Su, J., & Liu, L. (2000). SPH Simulation of River Ice Dynamics. Journal of Computational Physics, 165(2), 752-770.

Song, Y., Yan, J., Li, S., & Kang, Z. (2019). Peridynamic Modeling and Simulation of Ice Craters by Impact. Computer Modeling in Engineering & Sciences, 121(2), 465-492.

Sorsimo, A., Nyman, T., & Heinonen, J. (2016). Ship-ice interaction in a channel. The VTT Technical Research Centre of Finland, Helsinki, Finland.

Timco, G. W., & Weeks, W. F. (2010). A review of the engineering properties of sea ice. Cold Regions Science and Technology, 60(2), 107-129.

Vroegrijk, E. A. J. (2012). Application of the Discrete Element Method (DEM) on Ship-Ice Interaction. Paper presented at the SNAME 10th International Conference and Exhibition on Performance of Ships and Structures in Ice, Banff, Alberta, Canada.

Wang, C., Hu, X., Tian, T., Guo, C., & Wang, C. (2020). Numerical simulation of ice loads on a ship in broken ice fields using an elastic ice model. International Journal of Naval Architecture and Ocean Engineering, 12, 414-427.

Wang, C., Li, X., Chang, X., & Xiong, W. P. (2019). Numerical simulation of propeller exciting force induced by milling-shape ice. International Journal of Naval Architecture and Ocean Engineering, 11(1), 294-306.

Wang, J., Akinturk, A., Jones, S. J., & Bose, N. (2005). Ice Loads on a Model Podded Propeller Blade in Milling Conditions. 24th International Conference on Offshore Mechanics and Arctic Engineering, Halkidiki, Greece.

Wang, J., Akinturk, A., Jones, S. J., Bose, N., Kim, M.-C., & Chun, H.-H. (2006). Ice Loads Acting on a Model Podded Propeller Blade (OMAE2005-67416). Journal of Offshore Mechanics and Arctic Engineering, 129(3), 236-244.

Williams, F. M., & Spencer, D. (1992). Full scale trails in level ice with Canadian R-class icebreaker. The Society of Naval Architects and Marine Engineers, 100 (1992), 293–313.

Xie, H., Ackley, S. F., Yi, D., Zwally, H. J., Wagner, P., Weissling, B., Ye, K. (2011). Sea-ice thickness distribution of the Bellingshausen Sea from surface measurements and ICESat altimetry. Deep Sea Research Part II: Topical Studies in Oceanography, 58(9), 1039-1051.

Xiong, W. P., Wang, C., Wu, S., Ye, L. Y., & Xu, P. (2022). Study of different load components during the propeller-ice interaction process. Ocean Engineering, 247, 110787.

Yang, D., Liu, L., & Ji, S. (2023). Numerical analysis of interaction between sea ice and propeller based on coupled DEM-FEM model. Ocean Engineering, 268, 113469.

Ye, L. Y., Guo, C. Y., Wang, C., Wang, C. H., & Chang, X. (2020). Peridynamic solution for submarine surfacing through ice. Ships and Offshore Structures, 15(5), 535-549.

Ye, L. Y., Wang, C., Chang, X., & Zhang, H. Y. (2017). Propeller-ice contact modeling with peridynamics. Ocean Engineering, 139, 54-64.

Zhang, N., Zheng, X., Ma, Q., & Hu, Z. (2019). A numerical study on ice failure process and ice-ship interactions by Smoothed Particle Hydrodynamics. International Journal of Naval Architecture and Ocean Engineering, 11(2), 796-808.